First cycle voltage hysteresis in Li-rich 3d cathodes associated with molecular O_2 trapped in the bulk

Robert A. House[1,2,3,4], Gregory J. Rees[1,2,3,4], Miguel A. Pérez-Osorio[1,2,3,4], John-Joseph Marie[1,2,3,4], Edouard Boivin[1,2,3], Alex W. Robertson[1,2,3], Abhishek Nag[5], Mirian Garcia-Fernandez[5], Ke-Jin Zhou[5] and Peter G. Bruce[1,2,3,4,*]

1. Department of Materials, University of Oxford, Parks Road, Oxford, OX3 1PH, U.K.
2. Department of Chemistry, University of Oxford, South Parks Road, Oxford, OX1 3QZ, U.K.
3. The Henry Royce Institute, Parks Road, Oxford, OX1 3PH, U.K.
4. The Faraday Institution, Quad One, Becquerel Avenue, Harwell Campus, Didcot, OX11 0RA, U.K.
5. Diamond Light Source, Harwell, U.K.

*Corresponding Author, contact email: peter.bruce@materials.ox.ac.uk

Li-rich cathode materials are potential candidates for next generation Li-ion batteries. However, they exhibit large voltage hysteresis on the 1st charge/discharge cycle involving a substantial (up to 1V) loss of voltage and therefore energy density. For Na cathodes, e.g. $Na_{0.75}[Li_{0.25}Mn_{0.75}]O_2$, voltage hysteresis can be explained by formation of molecular O_2 trapped in voids within the particles. Here we show that this is also the case for $Li_{1.2}Ni_{0.13}Co_{0.13}Mn_{0.54}O_2$. RIXS and ^{17}O MAS NMR show that molecular O_2, rather than O_2^{2-}, forms within the particles on oxidation of O^{2-} at 4.6 V vs Li^+/Li on charge. These O_2 molecules are reduced back to O^{2-} on discharge but at the lower voltage of 3.75 V explaining the voltage hysteresis in Li-rich cathodes. ^{17}O MAS NMR indicates a quantity of bulk O_2 consistent with the O-redox charge capacity minus the small quantity of O_2 loss from the surface. The implication is that O_2, trapped in the bulk and lost from the surface, can explain O-redox.

Li-rich cathode materials, such as $Li_{1.2}Ni_{0.13}Co_{0.13}Mn_{0.54}O_2$ where Li:TM>1, are one of the very few options available to increase the energy density of Li-ion batteries.[1–3] Almost all of the lithium in these structures can be removed, compensated first by oxidation of the transition metal (TM) ions and subsequently the oxide ions, the latter at a constant potential of 4.6 V vs Li^+/Li.[4–10] However, the high voltage associated with this O-redox process on charge is not recovered on discharge leading to so called voltage hysteresis and a substantial loss of energy density. This represents one of the key challenges that has inhibited exploiting the full potential of these materials and the understanding of this phenomenon remains incomplete.

It is known that first cycle voltage hysteresis is related to structural change involving the migration of TM ions.[11–14] Recently, we explored O-redox in two Na intercalation compounds, $Na_{0.75}[Li_{0.25}Mn_{0.75}]O_2$ and $Na_{0.6}[Li_{0.2}Mn_{0.8}]O_2$, showing that formation of molecular O_2 and voltage hysteresis occurs in $Na_{0.75}[Li_{0.25}Mn_{0.75}]O_2$, which possess the honeycomb ordering of TM ions in the TM layer, but is suppressed in $Na_{0.6}[Li_{0.2}Mn_{0.8}]O_2$ with a ribbon superstructure ordering of TM ions in the TM layers.[15] However, the Li-rich O-redox compounds, such as $Li_{1.2}Ni_{0.13}Co_{0.13}Mn_{0.54}O_2$, which also possess a honeycomb ordering, are far more common, are of course relevant to Li-ion batteries and possess an O3 structure as opposed to the P2 structure of the Na compounds. Furthermore, it has been proposed that covalency, such as arising between the Ni/Co ions and the oxidised oxide ions, could serve to stabilise hole states on O, raising the question of whether the Li-rich O3 compounds would behave differently from $Na_{0.75}[Li_{0.25}Mn_{0.75}]O_2$. In particular, would the higher TM-O covalency suppress formation

of molecular O_2, perhaps favouring an explanation based on O_2^{2-} formation as suggested previously?[16–20]

Here, we investigate first cycle voltage hysteresis in $Li_{1.2}Ni_{0.13}Co_{0.13}Mn_{0.54}O_2$, an archetypal O3-type Li-rich cathode. We present evidence that O-redox is associated with the formation of molecular O_2 trapped in the bulk particles on charge, rather than peroxo-like species.[14,18,20,21] O_2 in the bulk is evidenced by high-resolution resonant inelastic X-ray scattering (HR-RIXS) spectroscopy and solid state ^{17}O magic angle spinning (MAS) nuclear magnetic resonance (NMR). T_1 NMR relaxation measurements show that the amount of O_2 in the bulk (~10 % of all O present) is commensurate with that expected from charging across the plateau (13 %) when corrected for the small amount of oxygen evolved from the surface. TM migration, primarily in-plane, forms voids that accommodate the O_2 molecules. On discharge, O_2 is reduced back to O^{2-} but the Li^+ returning to the TM layers do so into different sites resulting in O^{2-} coordinated by all Li^+ and O 2p states at higher energy leading to average discharge potential of 3.75 V vs. Li^+/Li, consistent with the voltage hysteresis. Oxidation of O^{2-} resulting in O_2 trapped in the bulk and O_2 evolved at the surface, together offer a unified explanation for O-redox. The balance between the two will depend on a number of factors including particle size/surface area and surface modifications/coatings.

$Li_{1.2}Ni_{0.13}Co_{0.13}Mn_{0.54}O_2$

$Li_{1.2}Ni_{0.13}Co_{0.13}Mn_{0.54}O_2$ was prepared via sol-gel synthesis as detailed in the Methods. The structure and composition were confirmed by powder X-ray diffraction (PXRD) and inductively coupled plasma - optical emission spectroscopy (ICP-OES), Supplementary Figure 1. $Li_{1.2}Ni_{0.13}Co_{0.13}Mn_{0.54}O_2$ crystallises with O3-type stacking of the oxide layers, Figure 1(a, b), and honeycomb ordering of the TM ions in the TM layers giving rise to the well-known superlattice peaks in PXRD, inset Fig. 1(d). Asymmetric peak broadening of the superstructure peaks is commonly observed amongst honeycomb ordered materials due to the presence of stacking faults.[22,23] The percentage of stacking faults in $Li_{1.2}Ni_{0.13}Co_{0.13}Mn_{0.54}O_2$ was determined at 20 % using DIFFaX,[24] Supplementary Figure 2(a).

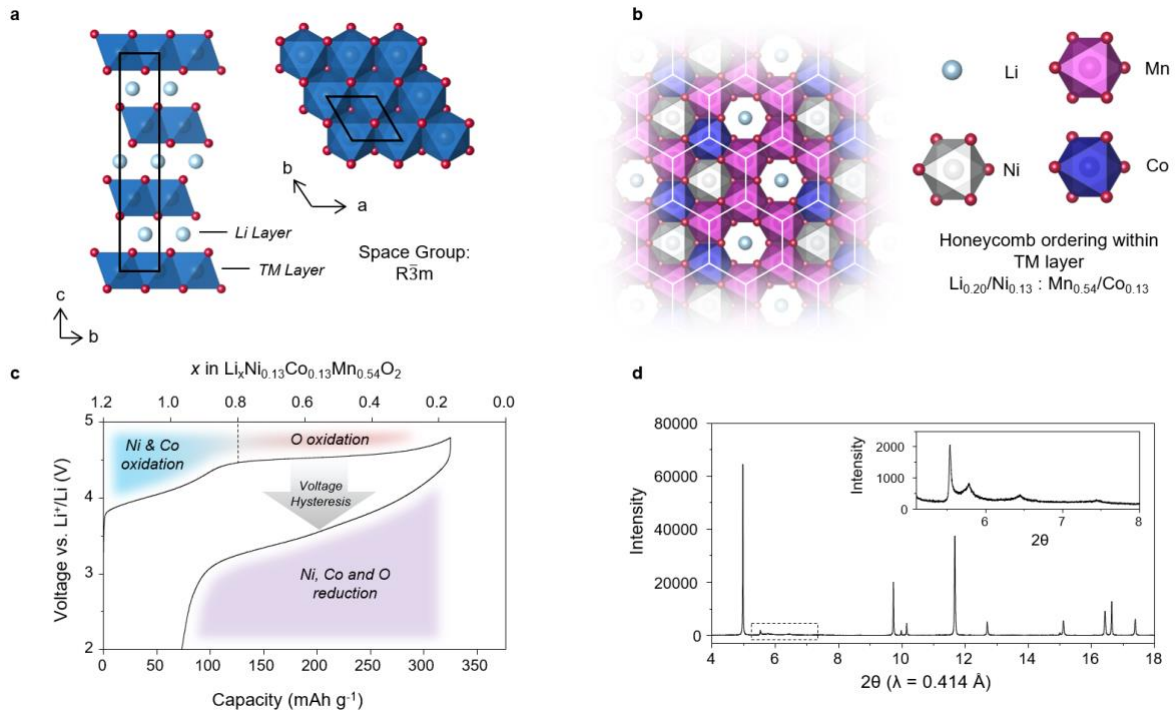

Fig. 1 Crystal structure and first cycle load curve *(a) $Li_{1.2}Ni_{0.13}Co_{0.13}Mn_{0.54}O_2$ with layered $R\bar{3}m$ crystal structure. (b) In-plane ordering of Li/Ni and Mn/Co within the transition metal layer gives rise to a honeycomb arrangement. The pictured configuration is one possible cation ordering scheme, which is used for DFT calculations later in this work (c) First charge-discharge cycle for $Li_{1.2}Ni_{0.13}Co_{0.13}Mn_{0.54}O_2$. (d) Synchrotron PXRD data showing diffraction peaks arising from honeycomb ordering inset.*

The first cycle charge-discharge profile, Figure 1(c) and Supplementary Figure 3, is similar to many other Li-rich cathodes including $Li_{1.2}Ni_{0.2}Mn_{0.6}O_2$, $Li_2Ru_{0.75}Sn_{0.25}O_3$ and $Li_2Ir_{0.5}Sn_{0.5}O_3$, with the initial sloping region, associated with oxidation of Ni and Co to +4, and then the voltage plateau at 4.6 V vs Li^+/Li associated with oxidation of the O^{2-} ions.[14,18,20,25] Subsequent discharge exhibits the well-known sloping S-shaped discharge at a much lower average potential than the charge plateau, i.e. voltage hysteresis. The O-redox plateau on charge contains a minor contribution from irreversible O-loss from the surface, the majority of the O-redox capacity on charge, 75%, is associated with bulk reversible O-redox, comensurate with the core-shell morphology and a thin 1-3 nm shell, Supplementary Figure 11. The sol-gel synthesised material exhibits comparable first cycle Coulombic Efficiency (~76% at 20 mA g^{-1}) to samples prepared by carbonate (~78% at 20 mA g^{-1})[26] and hydroxide (~76% at 25 mA g^{-1})[27] co-precipitation methods. Improved cycling efficiencies, >90%, have been demonstrated recently, especially through surface modification which can suppress irreversible O loss from the surface, shifting the balance towards even more reversible bulk O-redox.[27–29] Nevertheless, the issue of 1st cycle voltage hysteresis and the related nature of the oxidised O in the bulk i.e. of reversible O-redox, common to all these materials remains to be fully understood.

In-plane transition metal migration

A combination of *operando* PXRD, ^{6}Li MAS NMR and annular dark field – scanning transmission electron microscopy (ADF-STEM) was employed to follow the structural changes

on charge and discharge. The diffraction peaks arising from the in-plane TM honeycomb superstructure ordering reduce in intensity compared with the 001 peak on charging across the plateau and do not reappear on discharge, due to the loss of the honeycomb ordering, Figure 2(a) and Supplementary Figure 4. This irreversible loss of honeycomb ordering is also observed in the ADF-STEM images, Figure 2(b), which, along the [100] zone axis, show the disappearance of the 2 atom TM-TM dumbbells characteristic of TM honeycomb ordering within each TM layer on charging across the plateau. They do not reappear on discharge. While PXRD is sensitive to long range order, which is almost completely lost during charge, ADF-STEM shows that, on a local scale, disordering, although extensive, is not entirely complete throughout the whole material, Supplementary Figure 5. Rietveld refinement confirms that most of the TM disorder is in-plane, only a minority of the TM ions migrate to the Li layer (7% occupancy) at full charge (FC), Supplementary Figure 6, in line with previous studies.[13,30]

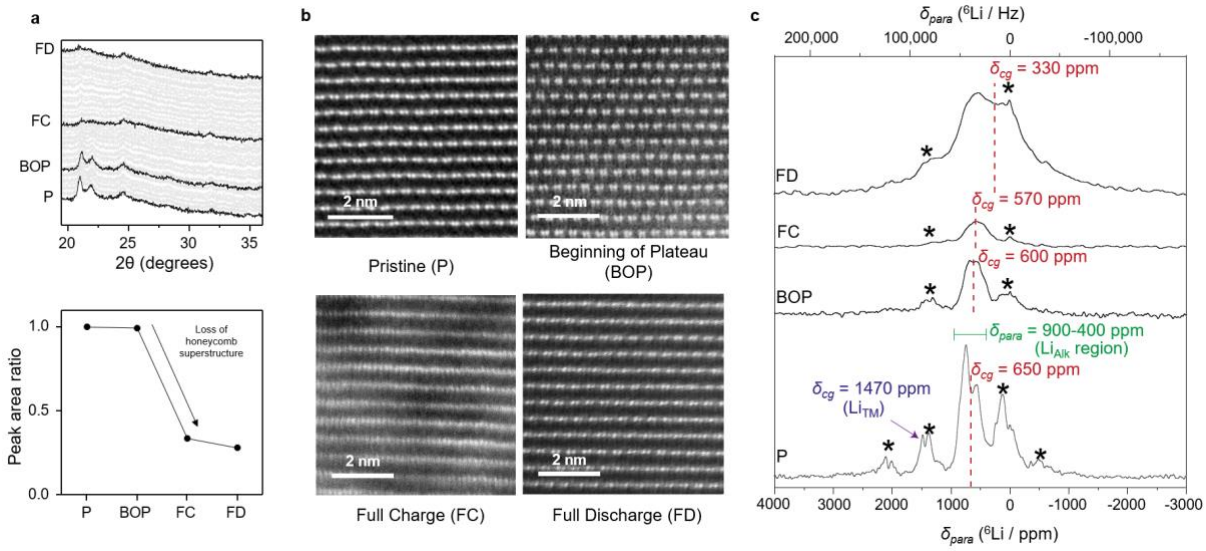

Fig. 2 Irreversible loss of honeycomb ordering *P (pristine), BOP (beginning of plateau), FC (Fully charged) and FD (fully discharged). (a) Operando X-ray diffraction of $Li_{1.2}Ni_{0.13}Co_{0.13}Mn_{0.54}O_2$ at different stages of the first charge-discharge cycle. The peak area ratio of the superstructure peaks relative to the 001 peak decreases across the plateau indicating loss of honeycomb ordering. (b) ADF-STEM images along the [100] zone-axis. Ni, Mn and Co are heavy scatterers and show up in white, Li is hardly visible in EM. The images show TM-TM dumbbells arising from honeycomb ordering within the TM layer are present in P and BOP but cannot be easily resolved in FC and FD indicating loss of in-plane ordering. (c) ^{6}Li NMR data for $Li_{1.2}Ni_{0.13}Co_{0.13}Mn_{0.54}O_2$. The resonance arising from Li in the TM layer (Li_{TM}) at 1470 ppm is in line with the presence of well-defined honeycomb ordering and those between 400 and 900 with Li in AM layers. However, in the FD sample the spectral density shifts to a lower centre of gravity (δ_{cg}) and is significantly broadened, the latter indicative of in-plane disorder and the former of clustering of Li. * denotes spinning sidebands.*

Solid state ^{6}Li MAS NMR is sensitive to the surrounding TM ions through their local hyperfine interactions. The sharp resonances in the spectra of the pristine material (P), Figure 2(c) indicate Li resides in highly ordered, well-defined sites, which have been previously assigned.[31,32] On charging to the beginning of plateau (BOP), the resonance at 1470 ppm decreases indicating removal of Li in the TM layer in line with previous NMR studies.[29] The

overall signal intensity continues to decrease on further charging until almost all the Li is removed from the structure, with very little detectable signal observed in the fully charged (FC) sample. At full discharge (FD), after lithium has returned to the structure, a significantly broader resonance is now evident than in the pristine state. This new signal is the sum of multiple NMR resonances from different local environments and indicates a much higher degree of disorder in the TMs surrounding Li, resulting from TM migration during charge. Furthermore, it is interesting to note that there is a substantial shift in the weighted centre of the spectra (from 750 to 330 ppm) between pristine and full discharge indicating that the Li environments are on average becoming more diamagnetic, consistent with clustering of the Li into more diamagnetic regions with fewer neighbouring TMs.

Formation and reduction of molecular O_2

To investigate the nature of oxidised O and its role in TM disordering and voltage hysteresis, high-resolution resonant inelastic X-ray scattering (RIXS), soft X-ray absorption spectroscopy (SXAS) and solid state ^{17}O MAS NMR were employed since they are direct probes of the electronic structure of O. Previous RIXS studies of O-redox materials have identified new characteristic emission features at 531 eV during O-redox, which are now believed to arise from the formation of short O-O bonds (<1.5 A).[33] However, determining the O-O species responsible for these has proven challenging due to their similarity with peroxide and oxygen references. Here, we access higher resolution RIXS data than before allowing us to assign the origin of these features. The data presented in Figure 3(a) show high-resolution O K-edge RIXS maps for pristine $Li_{1.2}Ni_{0.13}Co_{0.13}Mn_{0.54}O_2$ as well as at the beginning and end of the plateau, and their accompanying SXAS spectra. SXAS reveals the hole states on O, whereas, in RIXS, the incident radiation excites electrons from the O 1s states creating holes, and the subsequent emission arises from photons emitted by the relaxation of electrons from the filled oxygen valence states back into the core hole (O 1s) thus providing a direct probe of the oxygen valence states.

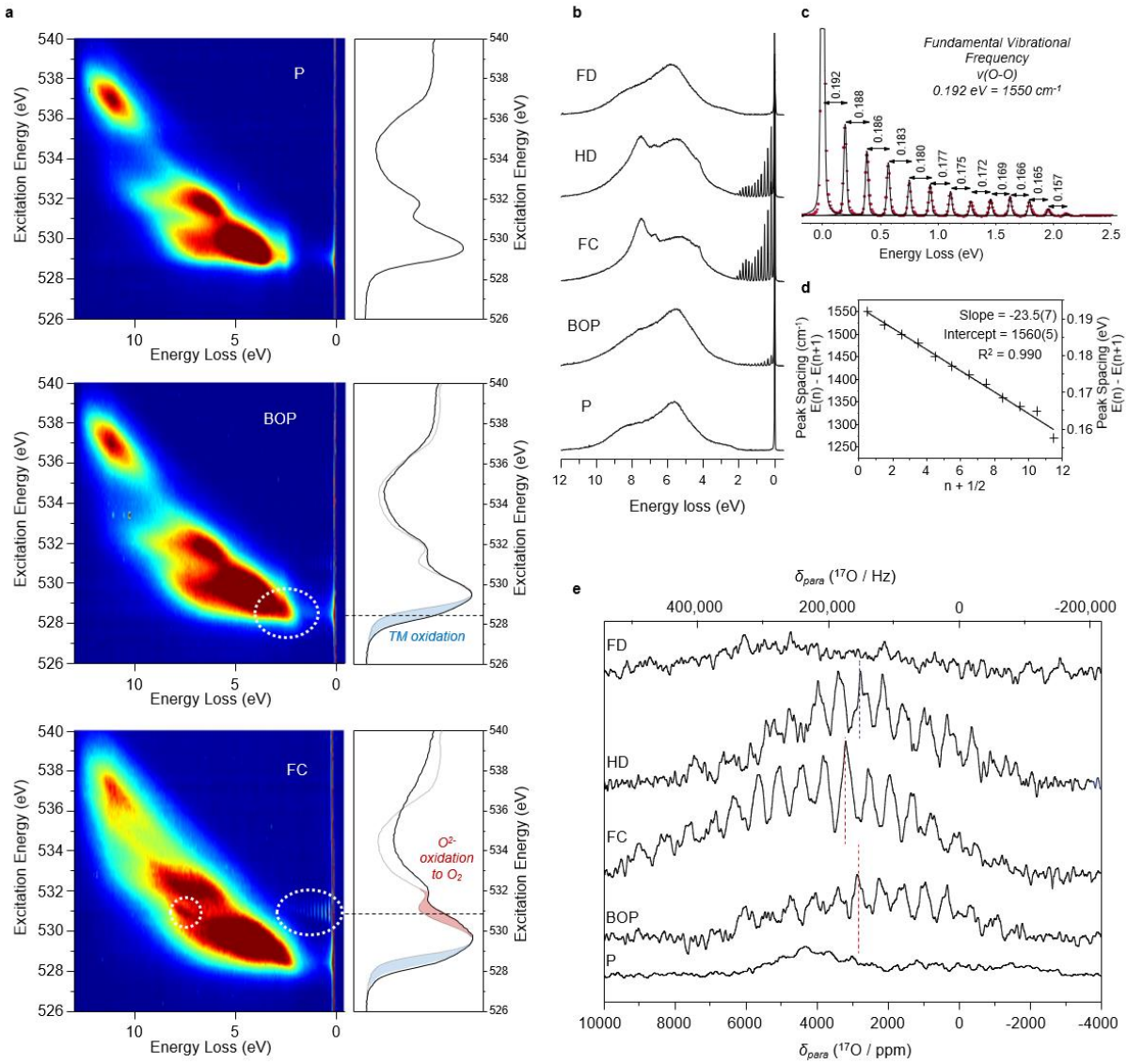

Fig. 3 Spectroscopic characterisation of O *(a) High-resolution RIXS maps and O K-edge Partial Fluorescence Yield (PFY) SXAS data for $Li_{1.2}Ni_{0.13}Co_{0.13}Mn_{0.54}O_2$. In RIXS, electrons are excited from the core hole (O 1s) states to the empty hole states and then photons emitted by the relaxation of electrons from lower energy valence states back into the core hole (O 1s) are detected. RIXS maps show the emission intensity plotted as a function of the energy lost between incident and emitted photons (x-axis) for different excitation energies across the O K-edge (y-axis). The SXAS spectra show the absorption intensity at the same corresponding excitation energies. At BOP, new electron holes are formed on the TM species (Ni and Co) leading to an increase in the area under the leading edge of the SXAS pre-edge. After the plateau at FC, new spectral weight appears in the middle of the SXAS pre-edge at 531 eV arising from electron hole states localised on molecular O_2. At this excitation energy, sharp energy loss features appear in RIXS from transitions to different electronic states on O_2. (b) High-resolution RIXS spectra at an excitation energy of 531 eV. (c) The low energy loss feature can be resolved into a progression of peaks arising from transitions to different vibrational energy levels corresponding the vibrational spectrum of molecular O_2. The separation between the first 2 peaks, or the fundamental vibrational frequency, is 0.192 eV, equivalent to 1550 cm^{-1}. (d) Birge-Sponer plot showing linear decrease in peak spacing characteristic of an anharmonic oscillating diatomic. 'n' is the vibrational quantum number. (e) Solid state ^{17}O MAS NMR spectra showing the formation of oxygen*

in a highly paramagnetically shifted environment (3000 ppm) which can be attributed to molecular O_2 trapped in the bulk of the cathode particles. The centre-band of the resonance, dashed peaks, shifts with the amount of O_2 present in the sample because of the change in bulk magnetic susceptibility (BMS). Dashed peaks are the paramagnetic centre bands (δ_{para}), the remaining peaks are spinning sidebands.

First, comparing the pristine and beginning of plateau, the additional hole states in the latter associated with Ni and Co oxidation on charging are evident centred at 528 eV in the SXAS, Fig 3(a). The corresponding RIXS spectra show that when excited at the same energy there is additional intensity in the RIXS emission spectrum, dotted circle in RIXS BOP map. On charging across the plateau, oxidation of oxide ions generates hole states on oxygen at 531 eV in SXAS. the corresponding RIXS maps at this excitation energy reveal clear changes highlighted by the dotted lines in the FC map, Figure 3(a). These represent new, oxygen valence states. Close inspection of the low energy loss feature close to the elastic peak, right hand dotted circle in FC RIXS map Figure 3(a), more clearly seen in the RIXS emission plot in Figure 3(b), reveals a progression of sharp peaks. When compared with the RIXS spectrum for molecular O_2, it is evident that the same sequence of peaks are present in both spectra.[34] They arise from transitions to different vibrational energy levels of an O-O diatomic.[35] The peak separation of the lowest energy loss peaks, Figure 3(c), corresponds to a fundamental vibrational frequency of 1550cm^{-1} consistent with that of molecular O_2 (~1556 cm^{-1})[36] and far from that of peroxo O_2^{2-} (~750 cm^{-1}).[37] The Birge-Sponer plot, Figure 3(d), shows that the peak spacing decreases linearly as a function of increasing energy loss confirming that they arise from transitions between different vibrational energy levels in an anharmonic potential well. At the end of discharge, FD in Figure 3(b), the spectral signature of O_2 is absent indicating reduction back to O^{2-}. Interestingly, some O_2 is still present even halfway along the discharge showing that O_2 is reduced continuously throughout the discharge process. The similarity in the vibrational frequency for O_2 in the structure with that of free O_2 suggests that any interactions with the Mn ions are small and the O_2 is best viewed as trapped within a cage. To investigate the possibility of the O_2 seen in RIXS arising from beam damage, spectra were collected under different temperature and beam flux conditions, Supplementary Figure 7. The data show no change to the peak spacing indicating the O-O bonding is not influenced by the beam. Furthermore, there is no evidence of an increase in intensity of the O_2 signal under harsher beam exposure as would be expected if the beam was inducing the O_2. Instead, there is a slight decrease consistent with previously reported data,[38] likely due to the loss of excited O_2 from the near surface of the particles into the surrounding ultra-high vacuum.

To independently verify the formation and reduction of molecular O_2, we employed MAS NMR on ^{17}O-labelled samples of $Li_{1.2}Ni_{0.13}Co_{0.13}Mn_{0.54}O_2$. Molecular O_2 is strongly paramagnetic, possessing two unpaired electrons, and as such is expected to have a significant paramagnetic relaxation enhancement (PRE) and also exhibit a large ^{17}O paramagnetic shift. As shown in Figure 3(d), by tailoring the NMR pulse sequence to bias for rapidly relaxing components (see Methods and Supplementary Figure 9), a new paramagnetic environment (~3000 ppm) can be detected in the fully charged samples, which is not present in either the pristine or fully discharged materials. The large shift is consistent with that expected for paramagnetic O_2 and the width of the sideband manifold matches closely with

that previously measured in condensed O_2.[39] The centre-band of the resonance, dashed peaks, shifts with the amount of O_2 present in each sample because of the change in bulk magnetic susceptibility (BMS). Furthermore, the presence of a ^{17}O sideband manifold, composed of a series of sharp peaks, indicates that molecular O_2 is rigidly caged within its local environment, consistent with the defect vacancy cluster. NMR is free from the effects of beam damage, thus confirming the validity of the RIXS measurements. Also, it is a bulk technique sampling all of the material. It should also be noted that RIXS, being a fluorescence technique, probes photons emitted from a depth of up to 50-100 nm into the sample, well beyond the thickness of any shell (typically approx. 2-5 nm), and therefore we do not expect any significant effects from near surface regions, although the NMR is valuable confirmation of this expectation.

The determination of the T_1 (spin-lattice) relaxation times for both the molecular O_2 and the bulk oxide environments reveals that approximately 10 % of the O in the fully charged (FC) cathode material is in the form of O_2, Supplementary Figure 10. From previous quantitative analysis of O-loss from $Li_{1.2}Ni_{0.13}Co_{0.13}Mn_{0.54}O_2$ by operando mass spec.,[6] it was determined that, of the 0.67 electrons (e^-) per formula unit (f.u.) associated with oxidation of oxide ions from beginning of plateau to full charge (4.8 V), 0.17 e^- per f.u. are associated with O extraction from the lattice and the other 0.5 e^- per f.u. are associated with oxidation of oxide ions that remain in the lattice. 0.5 e^- per f.u. results in 1/8th (12.5%) of the oxide ions being oxidised to O^0. However, O extraction reduces the total number of O atoms left in the structure from 2 to 1.91 per f.u (0.17 e^- per f.u. translates to loss of 0.09 O atoms per f.u.). Therefore, the percentage of O remaining in the sample that is in the form of O_2 based on the charge passed is predicted to be 13 %. Compared with Li_2MnO_3, where 100% of the O-redox capacity can be accounted for by irreversible O_2 evolution,[40] in $Li_{1.2}Ni_{0.13}Co_{0.13}Mn_{0.54}O_2$ only 25% of the O-redox capacity is lost as evolved O_2 despite the compound being 60% Li_2MnO_3 by composition ($0.6Li[Li_{1/3}Mn_{2/3}]O_2$-$0.4Li[Ni_{1/3}Co_{1/3}Mn_{1/3}]O_2$). This points to the important role of Ni and Co in activating bulk, as opposed to surface, O-redox.

TM disorder driven by O_2 formation

The above experimental data show that, on charging across the plateau, oxidation of oxide ions is accompanied by the formation of O_2 that remains in the material (i.e. O_2 in addition to the quantity lost from the lattice and detected by *operando* mass spec.). The formation of molecular O_2 inside the particles is only possible because of the loss of Li^+ from the TM layers and TM migration to form vacancy cluster defects that accommodate the O_2 molecules, i.e. the loss of the honeycomb superstructure. To explore the formation of vacancy cluster defects, O_2, and the energetics involved, Density Functional Theory (DFT) calculations were performed. To find a suitable model for the fully charged state, delithiated structures were prepared with different in-plane ordering schemes and their total energies calculated, Figure 4(a). Relative to the honeycomb ordered arrangement with Li^+ vacancies, most disordered configurations are comparable in energy, Figure 4(a). However, when the TM ions are arranged in such a way that the vacancies are clustered together, O_2 molecules spontaneously form during relaxation giving structures with substantially lower total energies. Out of all 60 computed configurations, the ground state configuration, Figure 4(b), containing a 4-vacancy

cluster and two O_2 molecules, was the lowest energy by almost 300 meV per f.u. compared with the rest. These results reveal a strong energetic driving force for the formation of molecular O_2 dependent on the migration of TM ions to form vacancy clusters.

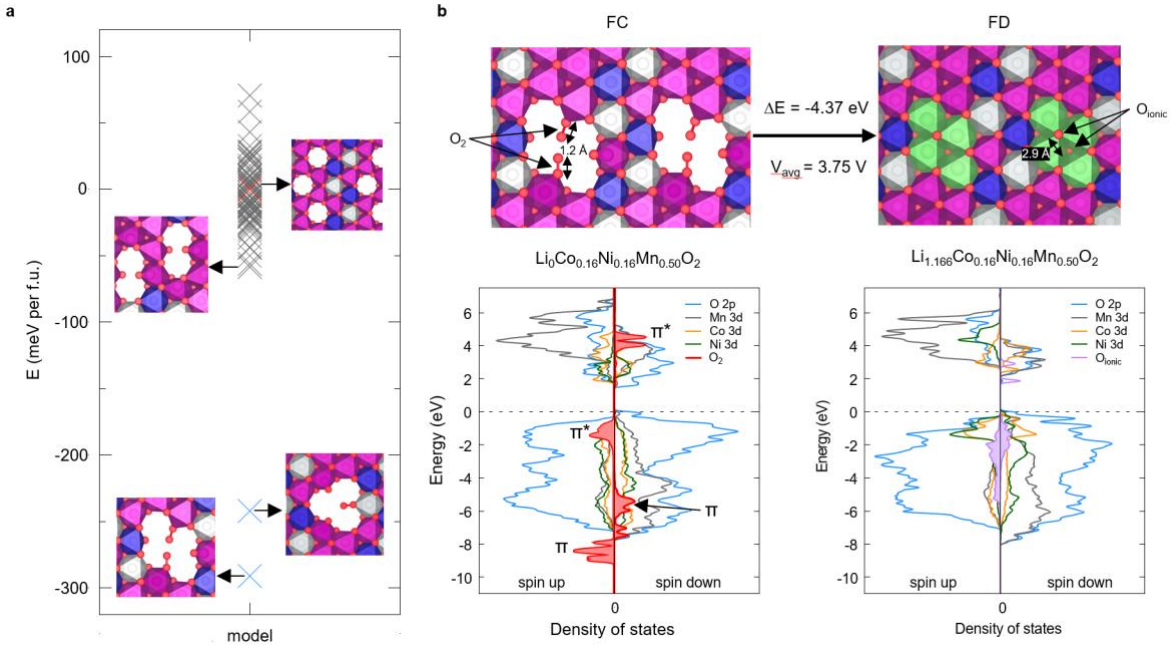

Fig. 4 Structural models for TM disorder and the discharge process *(a) Calculated total energies for fully delithiated $Li_{0.0}Ni_{0.16}Co_{0.16}Mn_{0.50}O_2$ with different orderings of vacancies and TM ions from Density Functional Theory (DFT). A total of 60 unique configurations were calculated out of all 500 non-symmetry-equivalent configurations. In red, a honeycomb ordered model which is taken as the reference energy. In grey, randomly sampled arrangements of the vacancies and TM without O_2. In blue and significantly lower in energy than any other arrangement, configurations where vacancies are clustered together allowing for the formation of O_2. (b) The average voltage of the discharge process associated with the reduction of O_2 molecules is calculated from DFT as 3.75 V using the lowest energy configuration for the charged structure. Below are the Density of States (DoS) plots for each structural model. In the FC, molecular O_2 gives clearly differentiated bands according to the molecular orbitals. In the FD, with a fully lithiated TM layer, the oxide ions surrounded by Li appear right at the top of the valence band and will be oxidised first during the second charge. In all DOS plots the Fermi level was set to zero.*

Bringing together the experimental data from RIXS and NMR, demonstrating formation of O_2, with the DFT calculations, the processes occurring on charging can be summarised as follows. On charging across the O-redox plateau, a two-phase reaction takes place between two fixed compositions before and after O oxidation. In the charged phase, upon oxidation of the oxide ions, the resulting species, nominally O^-, are unstable towards disproportionation triggering TM migration and forming O^{2-} and O^0 ($2O^- \rightarrow O^{2-} + O^0$). Two of these events results in two O^{2-} ions that are stabilised by coordination to 3 TM ions and two O^0 that dimerise to form O_2 molecules (1.2 Å) stabilised by the covalent bond formation. The molecular O_2 is rigidly caged within the vacancy cluster Figure 4(b). The formation of stable O^{2-} by coordination to 3 TM ions and stable O_2 provides the energetic driving force for the disproportionation of oxidised oxide ions and for the TM disordering.

To calculate the average voltage of the discharge process and determine if it is consistent with that observed electrochemically, we need to establish the structure at the end of discharge. On discharge, reduction of O_2 results in cleavage of the O-O bond and reformation of O^{2-} ions with an O-O distance of 2.5 Å and return of the Li^+ to the TM and Li layers, Figure 4(b). However, the returning Li^+ ions do not reoccupy the same sites but rather occupy the sites from which the TM ions have migrated.[15] The result is O^{2-} ions coordinated by Li^+ alone, as opposed to 2 TM and 1 Li in the pristine material. Using this discharged structure along with that of the charged state, an average voltage of 3.75 V vs Li^+/Li is calculated in close agreement with the experimentally observed discharge voltage.

From the Density of States (DoS) plot for the fully discharged structure, new filled states can be seen close to the Fermi Energy, Figure 4(b). These belong to O 2p states coordinated by Li^+ ions; the very weak (close to non-bonding) ionic interactions place the O 2p states high in energy, higher on average than the O 2p states for O^{2-} ions coordinated by 2 TM and a Li in the pristine material, Supplementary Figure 8. These will be oxidised first during the second charge at a lower potential than oxide ions in the honeycomb arrangement explaining the lack of voltage plateau on the second charge. RIXS data collected at the halfway point of the second charge, (HC) directly evidences this point, showing that even by 4 V substantial amounts of O_2 have already been generated, Figure 5(c).

Discussion

The observation that the 1st cycle voltage hysteresis in the Li-rich layered compound, $Li_{1.2}Ni_{0.13}Co_{0.13}Mn_{0.54}O_2$, involves formation of molecular O_2 on charge, similar to $Na_{0.75}[Li_{0.25}Mn_{0.75}]O_2$, demonstrates that the presence of Ni and Co in the TM layers and any resulting increase in covalency on the TM-O bond does not stabilise the hole states on oxidised oxide ions and does not lead to O_2^{2-} formation as reported previously.[14,16,18–20,41] The formation of O_2 molecules on charge is identified by RIXS and ^{17}O MAS NMR. The latter affords quantification of the amount of O_2, which agrees with the charge passed across the plateau (after accounting for the charge associated with the oxygen lost from the lattice). Also, the quantity of O_2 formed in the lattice, 13 %, is far more than evolved from the near surface on charging such materials. The sharp sidebands in the NMR signal for molecular O_2 is consistent with O_2 rigidly trapped in vacancy cluster defects within the particles, rather than O_2 in gas pockets between particles. Futhermore, it would be difficult for any O_2 outside the particles to re-enter and be reduced back to O_2^{2-} as is observed.

It is interesting to note that in many ways the early assumption that Li-rich compounds form O_2 on charge is correct. The difference is that we see O_2 forms throughout the particles; the relatively small amount of O_2 formed at the surface is lost, resulting in surface reconstruction to rocksalt/spinel like shell that inhibits further loss, the O_2 in the bulk is trapped in vacancy clusters, close to a TM centre, and can be reduced back to O^{2-} on discharge. While this latter process is reversible, the order-disorder transition that accompanies O_2 formation, resulting in the loss of honeycomb ordering and clustering of TM vacancies, is not. This structural rearrangement irreversibly changes the coordination environment around O. The Li^+ ions returning to the TM layer occupy the sites vacated by the TM ions, such that the O^{2-} ions in the discharged material are each now surrounded by Li^+ alone, as opposed to 2 TM and 1 Li^+

in the case of the pristine compound. As a result of the weak, close to non-bonding, interactions between the O^{2-} 2p states and Li^+, the former are higher in energy than when O^{2-} is coordinated by 2 TM and 1 Li^+, leading to a lower voltage on discharge compared with charge, i.e. voltage hysteresis, Figure 5.

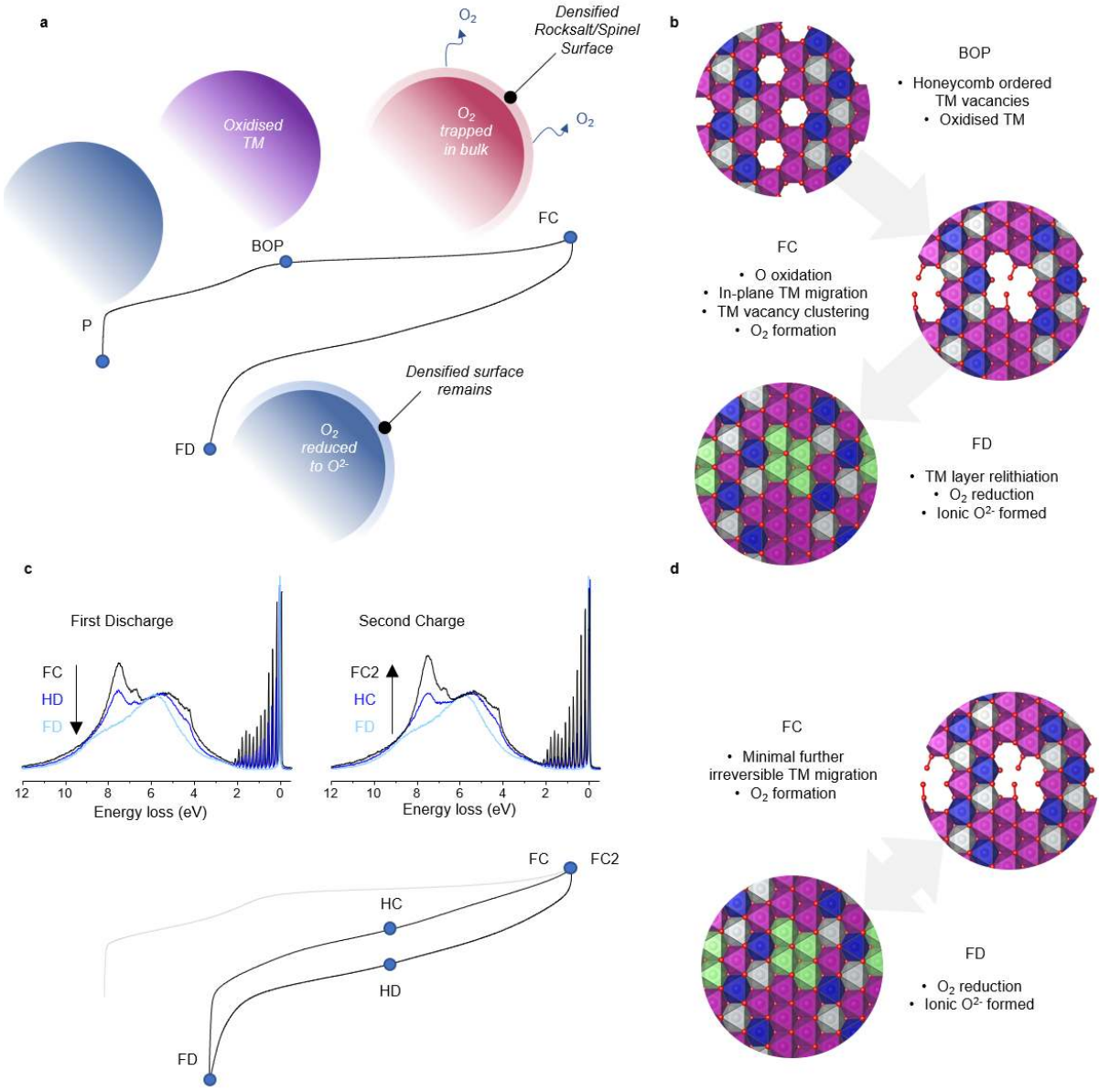

Fig. 5 Mechanism of 1st Cycle Voltage Hysteresis *(a) Macro-scale changes to the cathode particles: P to BOP, predominantly TM redox, some overlap with O-redox. Across the plateau O^{2-} is oxidised to form O_2 gas which is lost at the surface of the particles leading to surface densification (rocksalt/spinel), Supplementary Figure 11. O_2 formed in the bulk is trapped and can be reduced on discharge to reform O^{2-}. (b) Atomic-scale changes to ordering within the TM layer: BOP to FC, as O is oxidised in the honeycomb ordered TM layer, in-plane TM migration into the sites vacated by Li^+ is triggered. The most energetically favoured motif is the vacancy cluster, which allows for the formation of molecular O_2. Upon subsequent discharge Li^+ returns to the TM layers but now in different sites (occupied previously by TM ions). Structures shown are DFT models. (c) High-resolution RIXS spectra at 531 eV excitation energy showing the continuous reduction and formation of molecular O_2 throughout the first discharge and second charge respectively (first charge in grey). (d) Atomic-scale changes to TM layer after first*

charge. After the first cycle, vacancy clusters remain in the TM layer allowing for facile O_2 formation and reduction without requiring further TM migration. The presence of very ionic O atoms surrounded only by Li facilitates low voltage O oxidation, explaining the lack of plateau on second charge.

After relithiation on discharge, the newly formed disordered configuration is substantially higher in energy than the honeycomb ordered ground state (by about 250 meV per f.u. from our DFT calculations). However, reordering of the TM layer during the discharge process is not possible since the structure is rapidly repopulated by Li^+ ions which block TM migration. Nonetheless, it might be expected that moderate heating could provide enough thermal energy to overcome the kinetic barrier and recover the honeycomb order – and indeed this has been seen in very recent studies. Singer et al. showed that the voltage plateau on the 1st charge could be recovered by annealing cycled Li-rich NMC at moderate temperatures.[42] This annealing process was shown to recover the honeycomb ordering within the TM layer thereby reforming the coordination environment around O (2 TM/1 Li) conducive to high voltage O-redox.

The formation of O_2 on charging that leads to voltage hysteresis is only possible due to the disorder of the TM ions associated with the loss of the honeycomb structure thus forming vacancy clusters that accommodate O_2. One solution to achieving high voltage O-redox without voltage hysteresis is to allow O oxidation but inhibit TM migration and the formation of vacancy clusters. We recently showed that other ordering schemes, such as ribbon, are more stable than honeycomb and can provide much better support for oxidised O-ions.[15] This work, therefore, points the way toward a new strategy for the discovery of O3-type Li-rich materials whereby new vacancy ordering schemes within the TM layer may realise reversible high voltage O-redox. Understanding the nature of O-redox has proved a significant challenge for researchers, with many excellent contributions from different groups. The data presented in this work show strong evidence for O_2 trapped in the bulk of charged $Li_{1.2}Ni_{0.13}Co_{0.13}Mn_{0.54}O_2$ particles and its role in O-redox, including voltage hysteresis. Given the observation that quite small changes in the composition and structure of materials, e.g. from $Na_{0.75}[Li_{0.25}Mn_{0.75}]O_2$ to $Na_{0.6}[Li_{0.2}Mn_{0.8}]O_2$, can suppress voltage hysteresis, it will be interesting to examine other Li-rich cathodes with different compositions, particles sizes and/or higher cycling efficiencies to see if the same O_2 mechanism pertains.

Methods

Sol-gel synthesis Stoichiometric amounts of $LiCH_3COO.2H_2O$ (99.0% Sigma Aldrich), $Ni(CH_3COO)_2.4H_2O$ (99.0% Sigma Aldrich), $Co(CH_3COO)_2.4H_2O$ (99.0% Sigma Aldrich) and $Mn(CH_3COO)_2.4H_2O$ (99.0% Sigma Aldrich) were dissolved in 50mL of distilled water containing 0.1 mol of resorcinol (99.0% Sigma Aldrich), 0.15 mol of formaldehyde (Sigma Aldrich 36.5% in water) and 0.25 mmol of Li_2CO_3 (99.0% Sigma Aldrich). The mixture was stirred at 70 °C for 2 hours, then 500 °C for 5 hours, followed by calcination at 850 °C for 15 hours to obtain the product. All samples were handled under strictly anaerobic conditions to prevent degradation. They were transferred from the furnace to an Ar-filled glove box (H_2O and O_2 < 1ppm). ^{17}O-labelled samples were prepared in the same way except the final calcination step was performed under sealed atmosphere of O_2 gas (CortecNet >70 atom% ^{17}O).

Electrochemical Characterisation Electrodes were prepared by mixing 80 wt.% active material, 10 wt.% Super P carbon and 10 wt.% Polytetrafluoroethylene (PTFE) binder in a mortar and pestle and rolling to form self-supporting films. Electrodes were assembled into coin cells with electrolyte-soaked (1 M $LiPF_6$ in EC:DMC 50:50 (Battery Grade, Sigma Aldrich)) Whatman glass fibre separators and Li metal counter electrodes. Galvanostatic charge-discharge testing was carried out using Maccor Series 4000. The electrodes and cells were prepared and assembled/disassembled in the glove box under inert atmosphere and all cycling carried out under the same conditions.

Powder X-ray Diffraction Synchrotron diffraction data was collected from Advanced Photon Source, Argonne National Lab, 11-BM, through the rapid-access mail-in program. Operando diffraction data were collected on a Rigaku 9kW SmartLab Cu-source diffractometer equipped with Hypix 2D detector using an electrochemical cell with a beryllium window.

ADF-STEM micrographs were collected on an aberration corrected JEOL ARM 200F operated at 200 kV. The convergence semi-angle used was 22 mrad, and the collection semi-angle was 69.6–164.8 mrad (ADF). In all cases, sets of fast-acquisition multi-frame images were recorded and subsequently corrected for drift and scan distortions using SmartAlign.[43] Sample transfer to the STEM microscope was performed using a vacuum transfer suitcase to avoid exposure to air.

Spectroscopy High-resolution - Resonant Inelastic X-ray Scattering (HR-RIXS) data were collected from I21 beamline at Diamond Light Source. Scans at 531 eV were recorded at 5 different sample locations and averaged together, however, very little inhomogeneity in the signal was observed. Soft X-ray Absorption Spectroscopy (SXAS) data were recorded in partial fluorescence yield mode at i21 beamline, Diamond Light Source for the O K-edge. Sample transfer to the RIXS spectrometer was performed using a vacuum transfer suitcase to avoid exposure to air.

DFT Calculations Spin-polarized DFT calculations including Hubbard corrections (DFT+U) were carried out using the Quantum Espresso package.[44,45] The Perdew, Burke and Ernzerhof (PBE) exchange-correlation functional was employed.[46] Only valence electrons were explicitly described. The core-valence interaction was taken into account through the projector-augmented wave (PAW) method.[47] The wavefunctions and charge density were represented via plane-wave basis sets with energy cutoffs of 80 and 400 Ry, respectively. All calculations were performed considering a ferromagnetic ordering of the transition metal atoms. We use Hubbard parameters (U) of 4.0, 6.0 and 5.0 eV for Mn, Ni and Co 3*d* states, respectively. These values of U are similar to those reported for other closely related compounds. To find the *k*-point condition, the total energy of the supercell was converged with respect to the number of *k* points, and convergence was reached with a 2 × 2 × 3 Monkhorst–Pack *k*-point grid. Crystal structures were relaxed until forces on the atoms were less than 0.04 eV/Angstrom and the total stresses on the cell were less than 0.05 kBar. A supercell of the closely related compound $Li[Li_{0.1667}Co_{0.16}Ni_{0.16}Mn_{0.50}]O_2$, containing 96 atoms (28 Li atoms; 12 Mn atoms; 4 Co atoms; 4 Ni atoms; and 48 O atoms), was optimized and used an initial structure to investigate charge and discharge states. To investigate in-plane TM disorder in the charged phase, phases with different TM ordering were prepared using combinatorics. Simple random sampling (SRS) was used to choose a representative subset of non-symmetry equivalent configurations for relaxation. Fully delithiated models were considered to make calculations more computationally tractable.

On the top of the DFT+U simulations, we carried out hybrid calculations employing the Heyd–Scuseria–Ernzerhof (HSE) functional.[48] An exact exchange mixing parameter of 0.25 was used for all calculations. Norm-conserving pseudopotentials were used to describe the core-valence interaction. The electronic wavefunctions and charge density were described using plane-wave basis sets with an energy cutoffs of 80 and 320 Ry, respectively. A Monkhorst–Pack *k*-point grid of 2 × 2 × 3 was used.

The input structures were obtained from the DFT+U lattice optimizations, and the atomic positions were allowed to further relax at the HSE level, keeping the lattice parameters fixed.

Deintercalation-intercalation voltages V, were computed using the Nernst equation, which is given by

$$V = -\frac{\Delta G}{zF} \quad (1)$$

where ΔG is the Gibbs free energy change, F is the Faraday constant, and z is the charge that is transferred. First-principles calculations were carried out a 0 K and zero pressure. Under this conditions, the Gibbs free energy change is given by the change in the internal energy, ΔG=ΔE. Thus, deintercalation-intercalation voltages were computed as

$$V = -\frac{E(Li_{x1}TmO_2) - E(Li_{x2}TmO_2) - (x_1 - x_2)E(Li)}{(x_2 - x_1)F} \quad (2)$$

with $x_1 > x_2$

where $E(Li_{x1}TmO_2)$ and $E(Li_{x2}TmO_2)$ are the internal energies of the lithiated and delithiated transition metal (Tm) oxides, respectively, and E(Li) is the internal energy of metallic lithium.

Solid state ^{17}O and ^{6}Li MAS NMR The NMR samples were sealed in MAS rotors under an Ar environment and transferred to the magnet in a sealed inert atmosphere. The ^{17}O spectra (ν_0 = 54.3 MHz, 9.45 T) were acquired using a 250 kHz (1 µs, $\pi/2$) excitation pulse followed by a 125 kHz (2 µs, π) conversion pulse, separated by a $1/\nu_R$ delay, on Bruker 1.9 mm HXY probe achieving a MAS frequency of (ν_r =) 34 kHz spun using inert, dry N_2 gas. The data was acquired by variable offset cumulative frequency spectroscopy in 100 kHz steps and using a presaturation pulse comb to isolate the rapidly relaxing O_2 component (as detailed in Supplementary Figure 9). The ^{6}Li spectra (ν_0 = 58.9 MHz) were achieved using a 100 kHz ($\pi/2$) excitation pulse followed by a 50 kHz (π) conversion pulse and a ν_r = 36 kHz. All echoes were Fourier transformed as half-echoes using the Bruker Topspin (Billerica, MA) software and simulated using the DMFit.[49]

References

1. Croguennec, L. & Palacin, M. R. Recent achievements on inorganic electrode materials for lithium-ion batteries. *J. Am. Chem. Soc.* **137**, 3140–3156 (2015).

2. Croy, J. R., Balasubramanian, M., Gallagher, K. G. & Burrell, A. K. Review of the U.S. Department of Energy's 'deep Dive' Effort to Understand Voltage Fade in Li- and Mn-Rich Cathodes. *Acc. Chem. Res.* **48**, 2813–2821 (2015).

3. Hy, S. *et al.* Performance and Design Considerations For The lithium Excess Layered Oxide Positive Electrode Materials For Lithium Ion Batteries. *Energy Environ. Sci.* (2016). doi:10.1039/C5EE03573B

4. Koga, H. *et al.* Reversible Oxygen Participation to the Redox Processes Revealed for $Li_{1.20}Mn_{0.54}Co_{0.13}Ni_{0.13}O_2$. *J. Electrochem. Soc.* **160**, A786–A792 (2013).

5. Oishi, M. *et al.* Direct observation of reversible oxygen anion redox reaction in Li-rich manganese oxide, Li_2MnO_3, studied by soft X-ray absorption spectroscopy. *J. Mater. Chem. A* **4**, 9293–9302 (2016).

6. Luo, K. *et al.* Charge-compensation in 3d-transition-metal-oxide intercalation cathodes through the generation of localized electron holes on oxygen. *Nat. Chem.* **8**, 684–691 (2016).

7. Lu, Z., Beaulieu, L. Y., Donaberger, R. A., Thomas, C. L. & Dahn, J. R. Synthesis, Structure, and Electrochemical Behavior of $Li[Ni_xLi_{1/3-2x/3}Mn_{2/3-x/3}]O_2$. *J. Electrochem. Soc.* **149**, A778 (2002).

8. Johnson, C. S. *et al.* The significance of the Li_2MnO_3 component in 'composite' $xLi_2MnO_3{\cdot}(1-x)LiMn_{0.5}Ni_{0.5}O_2$ electrodes. *Electrochem. commun.* **6**, 1085–1091 (2004).

9. Seo, D.-H. *et al.* The structural and chemical origin of the oxygen redox activity in layered and cation-disordered Li-excess cathode materials. *Nat. Chem.* **8**, 692–697 (2016).

10. Saubanère, M., McCalla, E., Tarascon, J.-M. & Doublet, M.-L. The intriguing question of anionic redox in high-energy density cathodes for Li-ion batteries. *Energy Environ. Sci.* **9**, 984–991 (2016).

11. Lu, Z. & Dahn, J. R. Understanding the Anomalous Capacity of $Li/Li[Ni_xLi_{(1/3-2x/3)}Mn_{(2/3-x/3)}]O_2$ Cells Using In Situ X-Ray Diffraction and Electrochemical Studies. *J. Electrochem. Soc.* **149**, A815 (2002).

12. Armstrong, A. R. *et al.* Demonstrating Oxygen Loss and Associated Structural Reorganization in the Lithium Battery Cathode $Li[Ni_{0.2}Li_{0.2}Mn_{0.6}]O_2$. *J. Am. Chem. Soc.* **128**, 8694–8698 (2006).

13. Gent, W. E. *et al.* Coupling between oxygen redox and cation migration explains unusual electrochemistry in lithium-rich layered oxides. *Nat. Commun.* **8**, (2017).

14. Hong, J. *et al.* Metal-oxygen decoordination stabilizes anion redox in Li-rich oxides. *Nat. Mater.* **18**, 256–265 (2019).

15. House, R. A. *et al.* Superstructure control of first-cycle voltage hysteresis in oxygen-redox cathodes. *Nature* **577**, 502–508 (2020).

16. Xie, Y., Saubanère, M. & Doublet, M.-L. Requirements for reversible extra-capacity in Li-rich layered oxides for Li-ion batteries. *Energy Environ. Sci.* **10**, 266–274 (2017).

17. Yabuuchi, N. *et al.* Origin of stabilization and destabilization in solid-state redox reaction of oxide ions for lithium-ion batteries. *Nat. Commun.* **7**, 13814 (2016).

18. McCalla, E. *et al.* Visualization of O-O peroxo-like dimers in high-capacity layered oxides for Li-ion batteries. *Science* **350**, 1516–21 (2015).

19. Chen, Z., Li, J. & Zeng, X. C. Unraveling Oxygen Evolution in Li-Rich Oxides: A Unified Modeling of the Intermediate Peroxo/Superoxo-like Dimers. *J. Am. Chem. Soc.* **141**, 10751–10759 (2019).

20. Sathiya, M. *et al.* Reversible anionic redox chemistry in high-capacity layered-oxide electrodes. *Nat. Mater.* **12**, 827–35 (2013).

21. Foix, D., Sathiya, M., McCalla, E., Tarascon, J.-M. & Gonbeau, D. X-ray Photoemission Spectroscopy Study of Cationic and Anionic Redox Processes in High-Capacity Li-Ion Battery Layered-Oxide Electrodes. *J. Phys. Chem. C* **120**, 862–874 (2016).

22. Bréger, J. *et al.* High-resolution X-ray diffraction, DIFFaX, NMR and first principles study of disorder in the Li_2MnO_3–$Li[Ni_{1/2}Mn_{1/2}]O_2$ solid solution. *J. Solid State Chem.* **178**, 2575–2585

(2005).

23. Shunmugasundaram, R., Arumugam, R. S. & Dahn, J. R. A Study of Stacking Faults and Superlattice Ordering in Some Li-Rich Layered Transition Metal Oxide Positive Electrode Materials. *J. Electrochem. Soc.* **163**, A1394–A1400 (2016).

24. Treacy, M. M. J., Newsam, J. M. & Deem, M. W. A general recursion method for calculating diffracted intensities from crystals containing planar faults. *Proc. R. Soc. London. Ser. A Math. Phys. Sci.* **433**, 499–520 (1991).

25. Luo, K. *et al.* Anion Redox Chemistry in the Cobalt Free 3d Transition Metal Oxide Intercalation Electrode $Li[Li_{0.2}Ni_{0.2}Mn_{0.6}]O_2$. *J. Am. Chem. Soc.* **138**, 11211–11218 (2016).

26. Assat, G. & Tarascon, J. M. Fundamental understanding and practical challenges of anionic redox activity in Li-ion batteries. *Nat. Energy* **3**, 373–386 (2018).

27. Zhu, Z. *et al.* Gradient Li-rich oxide cathode particles immunized against oxygen release by a molten salt treatment. *Nat. Energy* **4**, 1049–1058 (2019).

28. Qiu, B. *et al.* ARTICLE Gas–solid interfacial modification of oxygen activity in layered oxide cathodes for lithium-ion batteries. *Nat. Commun.* **7**, (2016).

29. Zhao, E. *et al.* Local structure adaptability through multi cations for oxygen redox accommodation in Li-Rich layered oxides. *Energy Storage Mater.* **24**, 384–393 (2020).

30. Kleiner, K. *et al.* Origin of high capacity and poor cycling stability of Li-rich layered oxides - A long-duration in situ synchrotron powder diffraction study. *Chemistry of Materials* (2018). doi:10.1021/acs.chemmater.8b00163

31. Dogan, F. *et al.* Solid state NMR studies of Li_2MnO_3 and li-rich cathode materials: Proton insertion, local structure, and voltage fade. *J. Electrochem. Soc.* **162**, A235–A243 (2015).

32. Hua, W. *et al.* Structural insights into the formation and voltage degradation of lithium- and manganese-rich layered oxides. *Nat. Commun.* **10**, 1–11 (2019).

33. Gent, W. E., Abate, I. I., Yang, W., Nazar, L. F. & Chueh, W. C. Design Rules for High-Valent Redox in Intercalation Electrodes. *Joule* (2020). doi:10.1016/j.joule.2020.05.004

34. Arhammar, C. *et al.* Unveiling the complex electronic structure of amorphous metal oxides. *Proc. Natl. Acad. Sci.* **108**, 6355–6360 (2011).

35. Rubensson, J.-E., Pietzsch, A. & Hennies, F. Vibrationally resolved resonant inelastic soft X-ray scattering spectra of free molecules. *J. Electron Spectros. Relat. Phenomena* **185**, 294–300 (2012).

36. Weber, A. & McGinnis, E. A. The Raman spectrum of gaseous oxygen. *J. Mol. Spectrosc.* **4**, 195–200 (1960).

37. Radjenovic, P. M. & Hardwick, L. J. Evaluating chemical bonding in dioxides for the development of metal–oxygen batteries: vibrational spectroscopic trends of dioxygenyls, dioxygen, superoxides and peroxides. *Phys. Chem. Chem. Phys.* **21**, 1552–1563 (2019).

38. Lebens-Higgins, Z. W. *et al.* Distinction between Intrinsic and X-ray-Induced Oxidized Oxygen States in Li-Rich 3d Layered Oxides and $LiAlO_2$. *J. Phys. Chem. C* **123**, 13201–13207 (2019).

39. Dundon, J. M. ^{17}O NMR in liquid O_2. *J. Chem. Phys.* **76**, 2171–2173 (1982).

40. Rana, J. *et al.* Quantifying the Capacity Contributions during Activation of Li_2MnO_3. *ACS Energy Lett.* **5**, 634–641 (2020).

41. Li, X. *et al.* Direct Visualization of the Reversible O^{2-}/O^{-} Redox Process in Li-Rich Cathode Materials. *Adv. Mater.* **30**, 1705197 (2018).

42. Singer, A. *et al.* Nucleation of dislocations and their dynamics in layered oxide cathode materials during battery charging. *Nat. Energy* **3**, 641–647 (2018).

43. Jones, L. *et al.* Smart Align-a new tool for robust non-rigid registration of scanning microscope data. *Adv. Struct. Chem. Imaging* **1**, 8 (2015).

44. Cococcioni, M. & de Gironcoli, S. Linear response approach to the calculation of the effective interaction parameters in the LDA + U method. *Phys. Rev. B* **71**, 035105 (2005).

45. Giannozzi, P. *et al.* QUANTUM ESPRESSO: a modular and open-source software project for quantum simulations of materials. *J. Phys. Condens. Matter* **21**, 395502 (2009).

46. Perdew, J. P., Burke, K. & Ernzerhof, M. Generalized Gradient Approximation Made Simple. *Phys. Rev. Lett.* **77**, 3865–3868 (1996).

47. Blöchl, P. E. Projector augmented-wave method. *Phys. Rev. B* **50**, 17953–17979 (1994).

48. Heyd, J., Scuseria, G. E. & Ernzerhof, M. Hybrid functionals based on a screened Coulomb potential. *J. Chem. Phys.* **118**, 8207–8215 (2003).

49. Massiot, D. *et al.* Modelling one- and two-dimensional solid-state NMR spectra. *Magn. Reson. Chem.* **40**, 70–76 (2002).

Acknowledgements

P.G.B. is indebted to the EPSRC, including the SUPERGEN programme, the Henry Royce Institute for Advanced Materials (EP/R00661X/1, EP/S019367/1, EP/R010145/1, EP/L019469/1) and the Faraday Institution (FIRG007, FIRG008) for financial support. We acknowledge Diamond Light Source for time on I21 under proposal MM23889-1. Support from the EPSRC (EP/K040375/1 'South of England Analytical Electron Microscope') is also acknowledged. We acknowledge the resources provided by the Cambridge Tier-2 system operated by the University of Cambridge Research Computing Service (http://www.hpc.cam.ac.uk) funded by EPSRC Tier-2 capital grant EP/P020259/1, via the BATTDesign and AMAiB projects. The UK 850 MHz solid-state NMR Facility used in this research was funded by EPSRC and BBSRC (contract reference PR140003), as well as the University of Warwick including via part funding through Birmingham Science City Advanced Materials Projects 1 and 2 supported by Advantage West Midlands (AWM) and the European Regional Development Fund (ERDF).

Author Contributions

R.A.H. conceived and conducted the experimental work with contributions from J.J.M. and E.B.. G.J.R. collected, processed and interpreted the NMR data. M.A.P.-O. performed and interpreted the DFT calculations. A.W.R. performed the ADF-STEM measurements. R.A.H. and J.J.M. working closely with K-J. Z. and team A.N., M.G.F. conducted, processed and interpreted the RIXS and soft XAS measurements. R.A.H. and P.G.B. wrote the manuscript with contributions from all authors.

Competing Interest Statement

The authors declare no competing interests.

Data Availability Statement

Supporting research data has been deposited in the Oxford Research Archive and is available under this DOI:_____